

Highly stable, mesoporous mixed lanthanum–cerium oxides with tailored structure and reducibility

Shuang Liang · Esteban Broitman ·
Yanan Wang · Anmin Cao · Götz Veser

Received: 30 August 2010 / Accepted: 6 December 2010 / Published online: 17 December 2010
© Springer Science+Business Media, LLC 2010

Abstract Pure and mixed lanthanum and cerium oxides were synthesized via a reverse microemulsion-templated route. This approach yields highly homogeneous and phase-stable mixed oxides with high surface areas across the entire range of La:Ce ratios from pure lanthana to pure ceria. Surprisingly, all mixed oxides show the fluorite crystal structure of ceria, even for lanthanum contents as high as 90%. Varying the La:Ce ratio not only allows tailoring of the oxide morphology (lattice parameter, pore structure, particle size, and surface area), but also results in a fine-tuning of the reducibility of the oxide which can be explained by the creation of oxygen vacancies in the ceria lattice upon La addition. Such finely controlled syntheses, which enable the formation of stable, homogeneous mixed oxides across the entire composition range, open the path towards functional tailoring of oxide materials, such as rational catalyst design via fine-tuning of redox activity.

Introduction

Functional materials based on rare earth elements are of broad technological interest, and the synthesis of nanostructured rare earth oxides in particular, such as

nanostructured lanthanum and cerium oxides, has found increasing attention in recent years [1–4]. For example, nanostructured lanthana has been shown to be an outstanding absorbent for H₂S [5, 6] (a widely regulated air pollutant and a strong poison for typical metal catalysts [7, 8]), while ceria is widely investigated as catalyst support for noble metals in a number of reactions [9–13]. Beyond the pure oxides, growing interest is focusing on mixed cerium and other rare earth oxides [3, 14–21]. Doped lanthana nanoparticles are of interest as chemically stable photo-luminescent materials [22], and doped ceria shows strongly improved performance as catalyst support and oxygen storage component in applications such as automotive exhaust control [4, 9, 11, 18]. The latter is due to the fact that, unlike many traditional support materials, cerium oxide plays an important active role as oxygen storage and oxygen transfer material in redox reactions based on the facile conversion between Ce⁴⁺ and Ce³⁺. Doping ceria has been shown to further improve this performance due to increased reducibility and oxygen storage capacity. For example, computational studies have shown that doping ceria with Zr or Th cations lowers the reduction energy and increases the oxygen mobility [23]. More recent results indicate that La dopings are even more effective in favoring the Ce⁴⁺/Ce³⁺ reduction process than other trivalent dopants such as Sc, Mn, Y, Gd, and that this effect is enhanced with increasing La content [16].

Despite this interest in mixed La₂O₃–CeO₂ in particular, the synthesis of stable, homogeneous mixed oxides still poses a major challenge. The solubility limit for La₂O₃–CeO₂ mixed oxides prepared by various methods, including co-precipitation [24], solid state reaction [15], evaporation from solution [25], hydrothermal [26] and sol-gel synthesis [27], is typically below 40–70%, and even in

S. Liang · Y. Wang · A. Cao · G. Veser
US DOE-National Energy Technology Laboratory, Pittsburgh,
PA, USA

S. Liang · Y. Wang · A. Cao · G. Veser (✉)
Department of Chemical Engineering, University of Pittsburgh,
1249 Benedum Hall, Pittsburgh, PA 15261, USA
e-mail: gveser@pitt.edu

E. Broitman
Department of Chemical Engineering, Carnegie Mellon
University, Pittsburgh, PA 15213, USA

cases where the synthesis of mixed La_2O_3 – CeO_2 is successful, phase separation at elevated temperatures is commonly reported [28, 29]. This poses a significant limitation both with regard to technical application of such mixed oxides as well as to developing a deeper understanding of the impact of the oxide composition on material properties.

Here, we report the synthesis of nanostructured mixed La/Ce oxides via a straightforward reverse microemulsion-templated approach, and the systematic investigation of the La:Ce ratio on their reducibility. Reverse microemulsion-templated syntheses offer exceptional control over synthesis conditions [30, 31]. Confining the materials synthesis into the nanosized micelles not only allows regulation of particle size, and hence yields high surface area materials, but it also exerts control over the hydrolysis rate of different precursors for mixed oxides and hence allows for finely controlled synthesis of highly homogeneous mixed oxides with excellent thermal stability [32, 33]. Due to these well-controlled synthesis conditions, we were able to synthesize homogeneous mixed La/Ce oxides over the entire range of La:Ce ratios. The resulting oxides are characterized by high surface areas and, more importantly, exceptional stability with no phase separation up to temperatures in excess of 1000 °C. The full control of the composition furthermore enables fine tailoring of the reducibility of the materials.

Experimental section

Materials and syntheses

Chemical reagents including lanthanum isopropoxide (Alfa-aesar, La 40%), cerium isopropoxide (Alfa-aesar, Ce 37–45%), poly(ethylene glycol)-block-poly(propylene glycol)-block-poly(ethylene glycol) (PEPP, Aldrich, $M_n = 2000$), isoctane (Aldrich, 99.8%), 1-pentanol (Aldrich, 99+%), anhydrous 2-propanol (Aldrich, 99.5%) were used as received without further purification. Pure lanthanum oxide (La_2O_3), cerium oxide (CeO_2), and mixed lanthanum cerium oxides ($\text{La}_x\text{Ce}_{1-x}\text{O}_{2-0.5x}$) were all synthesized by a reverse microemulsion method, as adapted previously in our laboratory [34, 35]. For example, to prepare $\text{La}_{0.5}\text{Ce}_{0.5}\text{O}_{1.75}$, 10.97 g de-ionized water, 38.57 g isoctane and 12.85 g PEPP, 150 g 1-pentanol were used to obtain a reverse microemulsion. 0.5 g lanthanum isopropoxide and 0.59 g cerium isopropoxide were dissolved in 108 mL anhydrous 2-propanol by stirring, and refluxed at 95 °C for 2 h. The solution was then introduced to the microemulsion at room temperature. After aging for 72 h, the water and oil phases were separated by temperature-induced phase separation (TIPS). The product phase was washed several times with acetone, and remaining volatile

residues were removed via freeze drying. Finally, the dried powder was calcined at 450 or 750 °C for 2 h in air.

Characterization

The specific surface area was determined via nitrogen sorption in a Micromeritics ASAP 2020 gas adsorption analyzer using the BET method. Prior to the measurement, the samples were degassed for 2 h at 200 °C under high vacuum. The compositions of mixed oxides were determined by Energy-dispersive X-ray analysis (EDX) equipped on Philips XL-30 field emission scanning electron microscope (SEM). The X-ray diffraction (XRD) measurements were performed with a high-resolution powder X-ray diffractometer (Phillips PW1830) in line focus mode employing Cu K α radiation ($\lambda = 1.5418 \text{ \AA}$). Crystal phases were identified based on JCPDS cards. Particle sizes were calculated from the Debye–Scherrer equation. Sample morphology was determined by transmission electron microscopy (JEOL-2000FX). Temperature-programmed reduction by hydrogen (H₂-TPR) was conducted using a Micromeritics Chemisorb 2750 system equipped with a thermal conductivity detector. During the TPR analysis, the samples were first oxidized in 5% O₂/He at 450 °C for 2 h, and then TPR was performed by heating the sample (100 mg) at 5 °C/min to 900 °C in a 10% H₂/Ar flow (30 mL/min). A cold trap filled with acetone–dry ice mixture was placed between reactor and TCD to remove the water vapor.

X-ray photoelectron spectroscopy (XPS) spectra for samples containing different La concentrations were recorded in a Theta Probe system (Thermo Scientific) using a 400 μm diameter monochromatic Al K α excitation at 1486.6 eV with a Hemispherical Analyzer operated in the constant pass energy mode at 50 eV. To analyze the individual contributions of the Ce 3d and La 3d core levels, peak decomposition was carried out by using mixed Gaussian–Lorentzian peaks with a Shirley-type background.

Results and discussion

Pure oxides

Using the above described experimental approach, pure lanthanum and cerium oxides were first synthesized as reference points for the following synthesis and characterization of the mixed oxides. In particular for La_2O_3 reports of successful syntheses of high surface area materials are limited to-date [36, 37]. It seemed hence of interest in itself to investigate whether a carefully controlled microemulsion-based synthesis could result in increased surface areas.

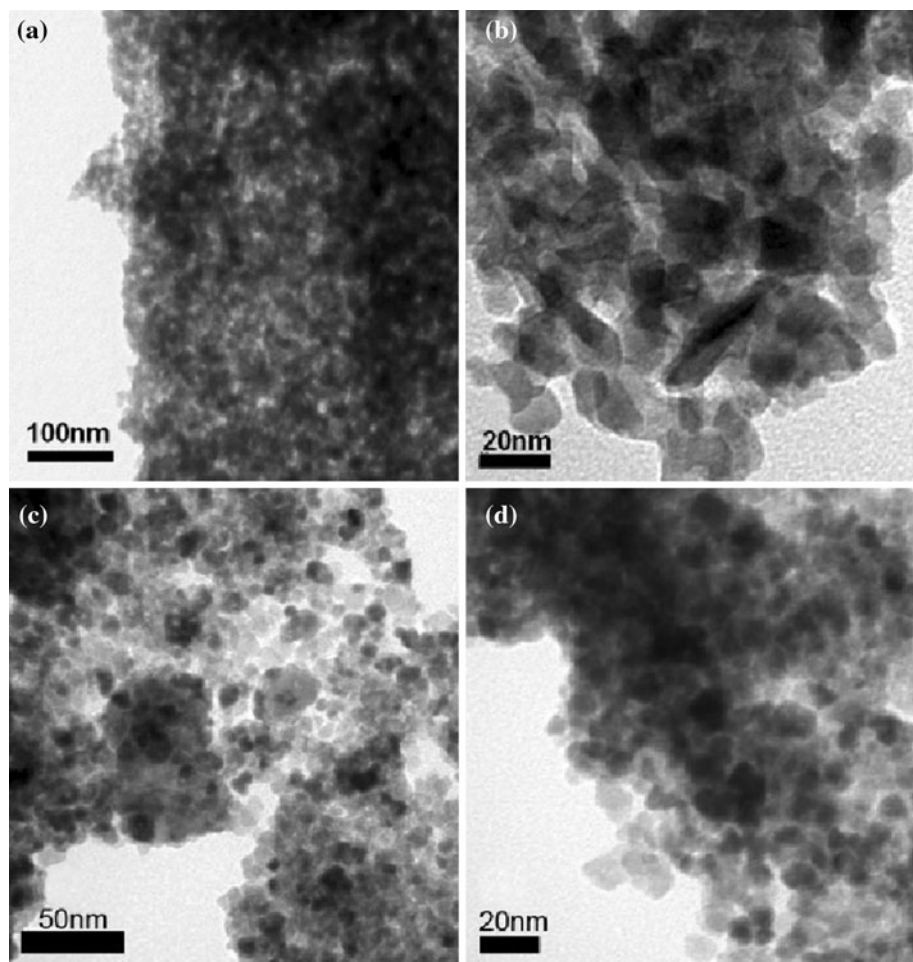
The morphology of pure La_2O_3 as synthesized in our microemulsion method is illustrated by the TEM images in Fig. 1a and b. The images reveal a mesoporous structure of the oxide, created by the agglomeration of dense nanoparticles about 10–20 nm in size. The mesoporous character of the materials is confirmed by BET, as seen in the typical type IV isotherms with H_2 hysteresis shown in Fig. 2 (top—a, b). The surface area of the lanthana is close to $100 \text{ m}^2/\text{g}$ after calcination at 450°C (see Table 1), well in excess of previously reported surface areas of less than $30 \text{ m}^2/\text{g}$ [38, 39]. XRD shows that the sample is largely amorphous after calcination at 450°C (Fig. 2top—c), in agreement with the known high crystallization temperature of La_2O_3 of $\sim 700^\circ\text{C}$ [5, 40, 41].

Cerium oxide synthesized in the same way shows a similar morphology and structure (Figs. 1c and d, 2bottom—a and b) and similarly high surface area of $\sim 80 \text{ m}^2/\text{g}$ (Table 1), which can be attributed to the small particle size templated by the micelles in the microemulsion. Unlike La_2O_3 , however, CeO_2 is already highly crystalline after calcination at 450°C , as confirmed by XRD

(Fig. 2bottom—c). It is worthwhile to note that, compared to La_2O_3 , the isotherm of CeO_2 calcined at 450°C (Fig. 2bottom—a) exhibits a different type H_2 hysteresis loop with a linear adsorption isotherm, indicating a highly disordered mesoporous structure with a wide pore size distribution [42, 43]. After high-temperature calcination at 750°C , the hysteresis loop changes to a type H1 hysteresis (Fig. 2bottom—b) attributed to agglomerates of spheres with roughly uniform size, resulting in narrow pore size distributions [42].

This change in structure upon high-temperature calcination also results in a strong decrease in surface area. As shown in Table 1, both pure oxides lose more than 70% of their surface area after calcination at 750°C due to rapid growth of the primary oxide particles. This strong sintering is not surprising for lanthana, which undergoes crystallization, resulting in large mass transport and hence restructuring of the material. However, a similarly large loss in surface area for ceria is less expected. It can most likely be attributed to the removal of residual surfactant that was capping the nanoparticles at lower temperature

Fig. 1 TEM image of crystallized La_2O_3 (a, b) and CeO_2 (c, d), after calcinations at 450 and 750°C , respectively



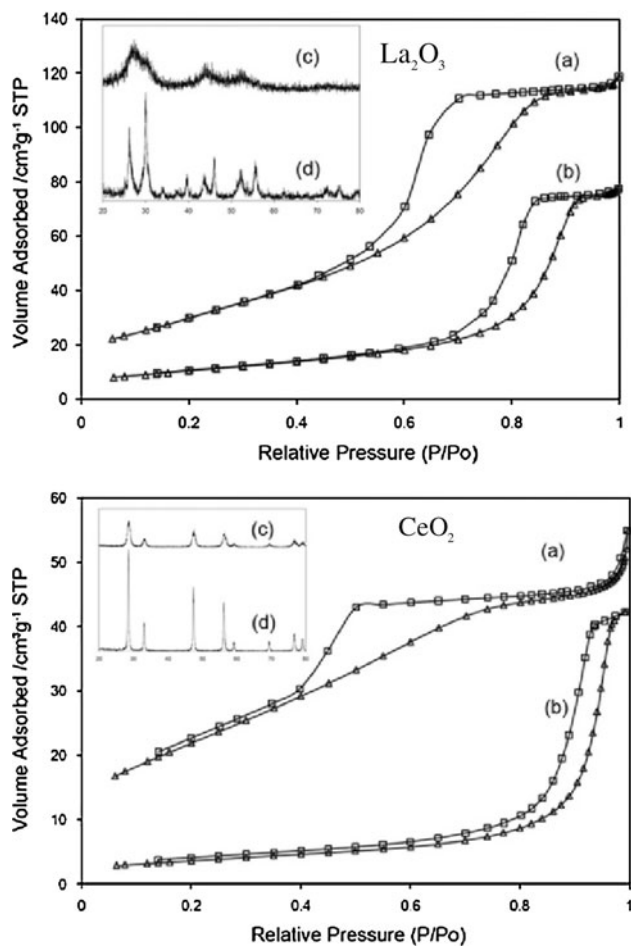


Fig. 2 Nitrogen adsorption–desorption isotherms for La_2O_3 and CeO_2 after calcined at 450 °C (a) and 750 °C (b), and XRD diffractograms for La_2O_3 and CeO_2 after calcined at 450 °C (c) and 750 °C (d)

and is being burnt off in the temperature range between 450 and 500 °C [34]. These cappings help to stabilize the materials at lower temperature by forming a diffusion barrier around individual nanoparticles, essentially “freezing” the materials in their disordered morphology resulting from the synthesis. After this barrier is burnt off at higher calcination temperatures, the particles start to sinter and rapid particle growth occurs (as confirmed by Debye–Scherer analysis, see Table 1). This can also explain the transition

in the nitrogen sorption hysteresis for ceria from an H2 to H1 hysteresis. However, despite this strong loss in surface area upon calcinations at 750 °C, the surface area of both pure oxides compares favorably with previous reports in the literature [30, 36].

Mixed lanthanum/cerium oxides

Based on the same microemulsion-templated synthesis used for the pure oxides, mixed La/Ce oxides were synthesized by using carefully adjusted mixtures of the respective precursors. The actual lanthanum and cerium content was determined via EDX and was found to be in close agreement with the nominal values from the synthesis (Table 2). For simplicity, we therefore use the nominal fractional La content ‘ x ’ to refer to the samples with different lanthanum content throughout the present report.

Figure 3 shows the TEM image along with the type IV isotherm with type H2 hysteresis loop for a mixed oxide with $\text{La}:\text{Ce} = 1:1$ after calcination at 450 °C. As expected, the mixed oxide shows no obvious difference in morphology and structure from either pure oxide.

Figure 4A shows the XRD diffractograms for pure and mixed $\text{La}_x\text{Ce}_{1-x}\text{O}_{2-0.5x}$ with increasing La content from 0% (i.e., pure ceria, Fig. 4A—a) to 100% (i.e., pure lanthana, Fig. 4A—g) after calcinations at 750 °C. The pure oxides show cubic and hexagonal crystalline structures for ceria and lanthana, respectively, in agreement with the standard XRD patterns of CeO_2 (JCPDS 34-0394) and La_2O_3 (JCPDS 05-0602). Surprisingly, however, all mixed oxides display only the (shifted) fluorite pattern of ceria (Fig. 4A—b–f), even for La loadings as high as 90%. No second phases or additional reflections can be found for any mixed oxide, indicating the formation of a single, homogeneous mixed-oxide phase. With increasing La content, however, one observes an increasing shift in the diffraction pattern, corresponding to a continuous change in the lattice parameter, as well as a broadening of the $\text{La}_x\text{Ce}_{1-x}\text{O}_{2-0.5x}$ reflections, indicating a decrease in particle size.

These trends are quantified in Fig. 4B, which shows the change of lattice constant and particle diameter as function of La content as calculated from the XRD patterns. One

Table 1 Surface area and particle size of La_2O_3 and CeO_2

450 °C			750 °C	
	Surface area (m^2/g)	Particle size (nm)	Surface area (m^2/g)	Particle size (nm)
La_2O_3	95.5	N.A. ^a	26.5	45.9
CeO_2	69.5	10.3	12.8	22.3

^a La_2O_3 calcined at 450 °C is amorphous and no particle size data can be acquired from XRD. TEM images in Fig. 1 allow estimate of particle size in the range of 10–20 nm

Table 2 Composition of mixed La/Ce oxides

La nominal fraction ‘x’	La actual at.% (from EDX)	Ce actual at.% (from EDX)
0.1	11.08	88.92
0.25	26.33	73.67
0.5	50.78	49.22
0.75	74.68	25.32
0.9	85.03	14.97

can see a continuous decrease in particle diameter with increasing La content, from ~22 nm for pure ceria to ~7 nm for 90% La content. This indicates that the addition of lanthanum suppresses the crystal growth of ceria, as previously observed by Wang et al. [6].

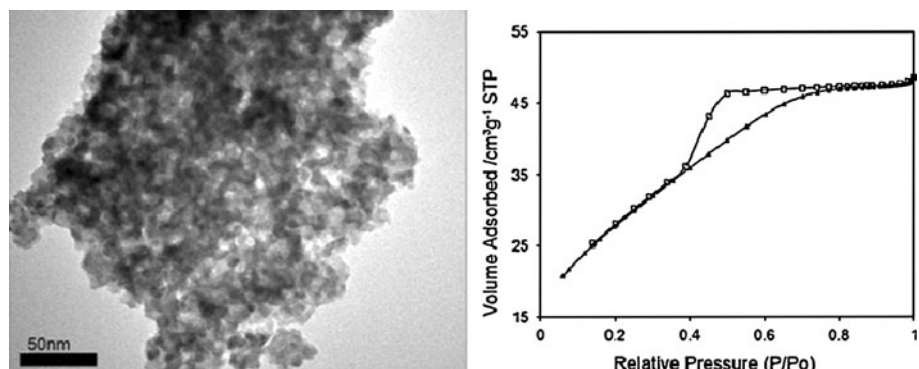
It should be noted here that both particle size and lattice strain can contribute to peak broadening in XRD, in particular for nanoparticles. Such lattice strain effects are accounted for by using a modified Scherrer equation [44, 45]: $\beta \cos\theta = 0.89\lambda/D + \eta \sin\theta$, in which β is full-width at half-maximum of the XRD peak, $\lambda = 1.5418 \text{ \AA}$ is the incident X-ray wavelength, θ is the diffraction angle, and D is the crystallite size. The latter can then be calculated by a linear fitting of $\beta \cos\theta$ versus $\sin\theta$. For our data, however, we found no dependence of $\beta \cos\theta$ on $\sin\theta$, with data scattering around a fixed value of $\beta \cos\theta$. We take this to indicate the absence of significant lattice strain in our samples, likely due to the high-temperature calcination at 750 °C. Therefore, average particle sizes were calculated directly from the simplified Debye–Scherrer equation, i.e.: $D = 0.89\lambda/(\beta \cos\theta)$.

Figure 4B, furthermore, shows that the lattice constant changes linearly from 5.41 Å for pure ceria to 5.70 Å for 90% La content, i.e., an overall increase of more than 5%. This linear increase in lattice constant is in agreement with previous calculations by Morris et al. [28]. However, this is the first time that a verification of these calculations up to high La content is possible, since previous attempts using various different synthesis strategies failed to do so due to

phase separation of a pure La_2O_3 phase at high La contents [15, 24–28]. This highlights the exceptionally well-controlled nature of the reported microemulsion-templated synthesis, which allows formation of mixed oxides across the entire range of La:Ce ratios.

The lattice expansion is further confirmed by HR-TEM (Fig. 5). Fast Fourier transformation (FFT) analysis of the HR-TEM image was used to identify the (111) plane and measure the lattice parameter of the oxide particles. It shows the expansion of the (111) d -spacing for high La-content mixed oxides from 0.318 nm for 50% La to 0.325 nm for 90% La content. For comparison, the value for CeO_2 (JCPDS 34-0394) is 0.311 nm (a comparison to La_2O_3 is not possible due to the different crystal structure). This lattice expansion can be attributed to a combination of the effects of increasing number of oxygen vacancies due to La doping and the larger ionic radius of La^{3+} versus Ce^{4+} [28, 46]. The HR-TEM images thus confirm the highly homogeneous, crystalline structure of these mixed oxides.

In order to further probe the phase stability of the high La-content mixed oxides, the samples were calcined at increasingly high temperature and characterized by XRD. Figure 6 shows the development of the XRD pattern for $\text{La}_{0.9}\text{Ce}_{0.1}\text{O}_{1.55}$ (i.e., 90% La) as a function of calcination temperature (a–c) in comparison to a pure ceria sample (d). One can see that the sample calcined at 450 °C shows only broad, weakly defined peaks at 28°, 47°, and 53°, which indicates the presence of very small crystallites. With increasing calcination temperature, these peaks get increasingly sharper and well-defined indicating particle growth as seen before for the pure oxides. However, all diffractograms are in perfect agreement with a shifted fluorite pattern for pure ceria (Fig. 6d). Most significantly, no additional reflections, which would suggest the formation of a separate La_2O_3 phase, are observed even after calcination at temperatures as high as 1050 °C. These results hence further confirm the formation of highly homogeneous mixed oxides, resulting in exceptional phase stability even at such extreme conditions. To our knowledge, this is the first report of such

Fig. 3 TEM image and nitrogen adsorption–desorption isotherms for $\text{La}_{0.5}\text{Ce}_{0.5}\text{O}_{1.55}$ calcined at 450 °C

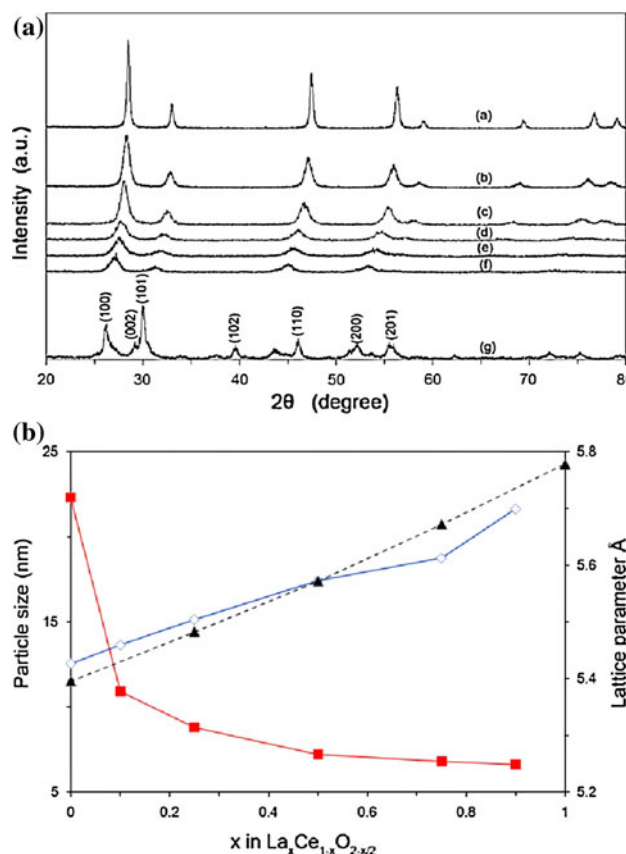


Fig. 4 **A** XRD of pure and mixed $\text{La}_x\text{Ce}_{1-x}\text{O}_{2-0.5x}$ calcined at 750 °C with La content (a) = 0%, (b) = 0.1, (c) = 0.25, (d) = 0.5, (e) = 0.75, (f) = 0.9, (g) = 1. **B** Experimental lattice parameter (empty diamond), calculated lattice parameter (solid triangle), and particle size (solid square) of $\text{La}_x\text{Ce}_{1-x}\text{O}_{2-0.5x}$ with different La content after calcined at 750 °C

highly stable mixed oxides over a broad range of La contents as high as 90%.

The exceptional homogeneity and stability of the mixed oxide phase can be attributed to the controlled synthesis. Unlike co-precipitation or non-templated sol-gel methods, the rate of microemulsion-templated syntheses is determined by the diffusion of the precursors from the oil phase

into the aqueous phase rather than by precipitation or hydrolysis which tend to be very rapid and hence poorly controlled [32]. The similar diffusivity of the two alkoxide precursors in the oil phase results in similar (effective) reaction rates and hence in well-ordered materials in which the composition on the atomic scale reflects the well-mixed composition of the precursor solution.

However, at this point, we do not have a clear explanation why the mixed oxide phases favor the fluorite crystal structure even for La contents as high as 90%. One possible explanation could be that the amorphous mixed oxide starts crystallizing in the fluorite-type structure during calcination at low temperatures, since the crystallization temperature of ceria (<450 °C) is much lower than that of lanthana (~700 °C), and, once formed, the above discussed homogeneity of the materials results in stabilization this structure. This is supported by the development of the XRD patterns during the crystal growth process of the mixed oxide (see Fig. 6). However, more work is required to fully elucidate this point, and particularly computational materials modeling of these mixed oxides could shed further light on this surprising observation.

In addition to crystal structure, the surface area of the mixed oxides is also affected by the La content. Figure 7 shows the BET surface area of pure and mixed $\text{La}_x\text{Ce}_{1-x}\text{O}_{2-0.5x}$ oxides versus lanthanum content after calcinations at 450 and 750 °C. At both temperatures, the mixed oxides have significantly higher surface areas than either pure oxide. For example, after calcination at 450 °C the surface area of $\text{La}_{0.25}\text{Ce}_{0.75}\text{O}_{1.875}$ is 113 m²/g, i.e., approximately twice the surface area of pure La_2O_3 or pure CeO_2 . Furthermore, as expected from the results for the pure oxides, the surface area for all samples drops sharply after calcination at 750 °C for 2 h. For example, the specific surface area of mixed oxides with a La content between 10 and 50% drops from ~110 m²/g at 450 °C to ~30 m²/g at 750 °C, i.e., the materials lose over 70% of their surface area. This is consistent with the results for the pure oxides and suggests again that the loss of the residual surfactant capping in this temperature range results in particle growth.

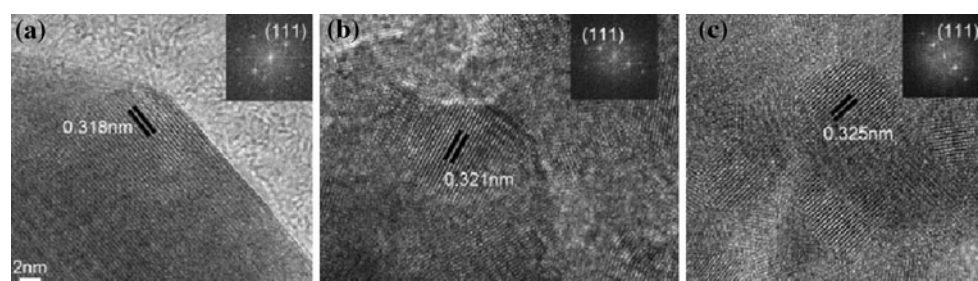


Fig. 5 HR-TEM images of $\text{La}_x\text{Ce}_{1-x}\text{O}_{2-0.5x}$ with $x = 0.5$ (a), $x = 0.75$ (b), $x = 0.9$ (c) (insets show the fast Fourier transformation patterns of the respective HR-TEM image)

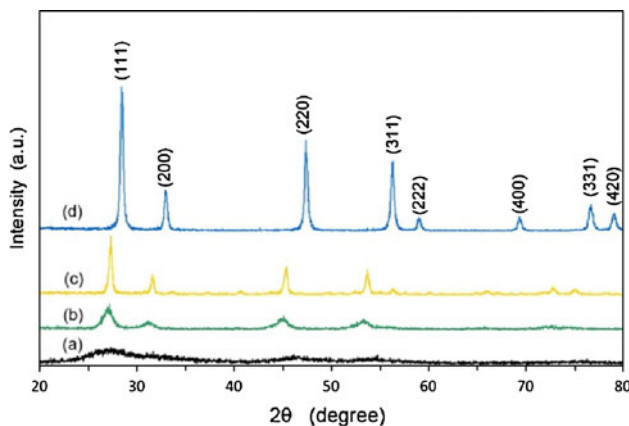


Fig. 6 XRD of $\text{La}_{0.9}\text{Ce}_{0.1}\text{O}_{1.55}$ (a) calcined at 450 °C, (b) 750 °C, (c) 1050 °C, (d) CeO_2 calcined at 750 °C

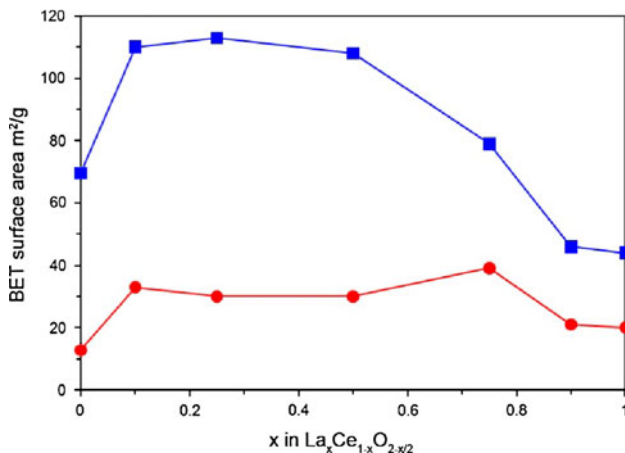


Fig. 7 BET surface area of $\text{La}_x\text{Ce}_{1-x}\text{O}_{2-0.5x}$ with different lanthanum content, aged at 450 °C (solid square) or 750 °C (solid circle)

However, the mixed oxides still remains roughly twice the surface area of either of the pure oxides. Finally, it is interesting to note that even relatively small La additions to ceria (see 10% La in Fig. 7) result in a drastic increase in surface area, while the addition of small amounts of Ce to lanthana (90% La) has comparatively little impact on the surface area. Clearly, La plays a much more important role in stabilizing high surface areas than Ce.

Beyond surface area, the porosity has a decisive impact on the performance of materials in applications such as sorption, sensing, and catalysis. The pore size distributions of the mixed oxides were hence determined from nitrogen adsorption isotherms using the BJH method. It is worth noticing that the desorption branches of the isotherms of the mixed oxides show a lower closure point at $p/p^0 = 0.4$ –0.45, in which case the pore size distribution obtained from the adsorption branch of the isotherm is

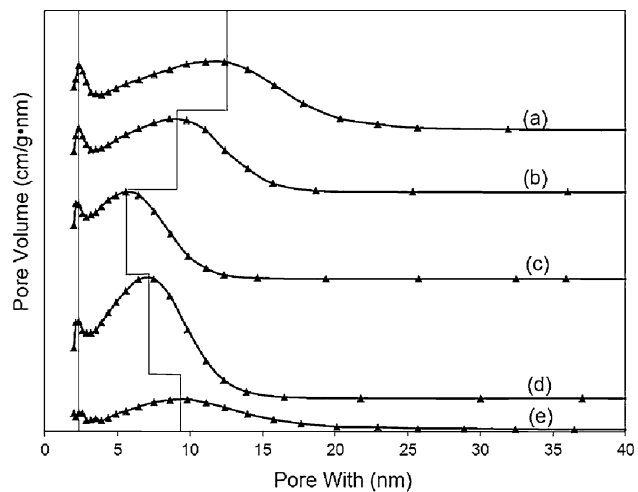


Fig. 8 BJH pore size distributions obtained from the adsorption branches of the isotherms of $\text{La}_x\text{Ce}_{1-x}\text{O}_{2-0.5x}$ with varying La content after calcinations at 750 °C for 2 h in air: (a) = 0.1, (b) = 0.25, (c) = 0.5, (d) = 0.75, (e) = 0.9

considered more reliable and was hence used here [42, 43]. Figure 8 shows the results for mixed oxide samples with (a) 10%, (b) 25%, (c) 50%, (d) 75%, and (e) 90% La content. One can see an interesting development of a bimodal pore size distribution as function of La content: The 10% La sample (Fig. 8a) shows a bimodal distribution with a weak peak at 2.3 nm (“peak I”), and a more pronounced, broader peak at 12 nm (“peak II”). Peak I maintains its position at 2.3 nm for all samples. However, upon increasing the La content to 25 and 50%, peak II shifts continuously towards lower pore diameters and sharpens noticeably, while at La loadings above 50%, it broadens again and shifts back towards larger pore diameters.

This observation seems to suggest that mixed $\text{La}_x\text{Ce}_{1-x}\text{O}_{2-0.5x}$ oxides contain two types of pores, both in the mesopore range. One type of pores has a diameter of 2.3 nm and appears unaffected by the La:Ce ratio, while the diameter of the second type of pores and its relative contribution to the total pore volume is strongly determined by the La content. Furthermore, the second type of pores dominates the pattern when the lanthana content is adjusted to either direction away from 50%. While it is tempting to interpret the occurrence of these two types of pores due to the formation of two different oxide phases, this is clearly contradicted by our results from XRD and TEM investigations, as described above. At this point, we do not have a consistent explanation of this phenomenon. Further investigations appear worthwhile, however, as this suggests a simple way to tailor the pore size for these mixed oxides without a strong impact on surface area (see Fig. 7).

Reducibility of pure and mixed oxides

Finally, the reducibility of the mixed oxides was investigated via H₂ temperature programmed reduction. Reducibility and oxygen storage capacity are key functional properties of oxide materials, particularly for ceria which is widely used as oxygen storage and “transfer” agent in catalysis and related applications [47–50]. As discussed before, it can be expected that the reducibility of these mixed oxide samples is strongly affected by the La content due to the introduction of oxygen vacancies.

The TPR patterns are shown in Fig. 9a, and Table 3 summarizes the respective peak positions, peak areas and H₂ consumptions for all samples after calcination at 750 °C. Pure ceria shows a low-temperature reduction peak at 420 °C, which can be attributed to the reduction of surface oxygen, and a high temperature reduction peak

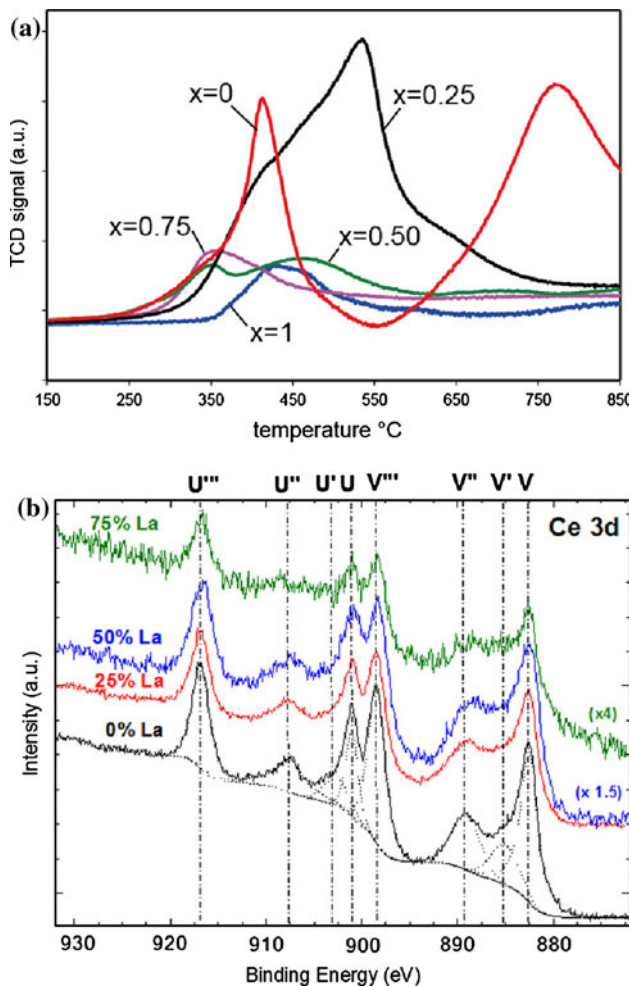


Fig. 9 **a** H₂-TPR profiles of La_xCe_{1-x}O_{2-0.5x} with different lanthanum content (x). **b** The Ce 3d spectra for samples with different amounts of La content. Solid lines represent the experimental spectra and the dotted lines in the CeO₂ sample are the Shirley background and the results from peak fitting

Table 3 Reduction temperature and hydrogen consumption

	Peak position (°C)	Peak area (a.u.)	H ₂ consumption (μmol/g)
CeO ₂	420	5.12	395.5
La _{0.25} Ce _{0.75} O _{1.875}	500	13.36	1022.0
La _{0.5} Ce _{0.5} O _{1.55}	350	1.71	135.6
La _{0.75} Ce _{0.25} O _{1.625}	350	1.70	135.5
La ₂ O ₃	430	1.08	88.2

above 700 °C, which is due to the (less facile) bulk reduction. In contrast, the mixed oxide with 25% La content shows only one, broad, strongly enhanced reduction peak, indicating a strong increase in the number of available oxygen species and more easily accessible bulk oxygen. This is in good agreement with the expected effect of La addition, as discussed above. As the La content increases further, the reduction peak shifts towards lower temperature, indicating increasingly facile reduction of the sample. However, the H₂ consumption of the samples with 50 and 75% La content decreases dramatically (see Table 3), indicating a strong decrease in the number of reducible sites.

The impact of La on the reducibility of ceria was further investigated by X-ray photoelectron spectroscopy (XPS). Figure 9b shows the Ce 3d spectra for four different oxide compositions (0, 25, 50, and 75% La). There are 8 peak assignments in the spectra, which are labeled according to the convention established by Burroughs [51]. The peaks U, U', U''' and V, V'', V''' refer to 3d_{3/2} and 3d_{5/2}, respectively, and are characteristic of Ce⁴⁺ 3d states. The peaks U', V' refer to 3d_{3/2} and 3d_{5/2}, respectively, and are characteristic of Ce³⁺ 3d final [51]. The fitted peak contributions and background are indicated by dotted lines for the pure CeO₂ sample. The doublets V⁰ and U⁰, corresponding to the Ce³⁺ 3d⁹ 4f¹ O 2p⁶ final state, typically located at 880.6 and 898.9 eV, do not appear in our samples, indicating that Ce is mostly present in the Ce⁴⁺ oxidation state [52].

The ratio between Ce⁴⁺ and Ce³⁺ was calculated from the contributions in the XPS spectra, based on the above described peak assignments and the following equations:

$$\text{Ce}^{4+} = (U + U'' + U''' + V + V'' + V''') / \left[\sum_{n'} (U^{n'} + V^{n'}) \right] \quad (1)$$

$$\text{Ce}^{3+} = (U' + V') / \left[\sum_{n'} (U^{n'} + V^{n'}) \right] \quad (2)$$

where n' is for all states [52]. Using this method, the fitted peak areas in the XPS spectra were used to estimate the contributions of Ce⁴⁺ and Ce³⁺ as well as sample

Table 4 Atomic composition of samples and their Ce⁴⁺/Ce³⁺ ratio

La % (nominal)	Ce ⁴⁺ /Ce ³⁺	Composition by XPS	
		Ce at.%	La at.%
0	4.97	24.55	0.00
25	6.47	17.82	9.15
50	7.22	13.93	18.02
75	13.67	4.25	17.13

composition (Table 4). The values obtained for sample composition are in reasonable agreement with the nominally expected values as well as values determined from EDX (cp. Table 2). The difference between the compositions as determined from XPS and the nominal compositions indicates that the surface of the mixed oxide particles are slightly enriched in lanthanum, in particular for low La contents [24].

More importantly, one can see that the data shows a strong increase in Ce⁴⁺/Ce³⁺ ratio with increasing La content, from 4.97 for pure CeO₂ to 13.67 at 75% La. This suggests that La³⁺ is substituting Ce³⁺ ions in the ceria lattice, hence resulting in an increase of the Ce⁴⁺/Ce³⁺ ratio. However, since the La amount in all samples exceeds the amount of reduced Ce³⁺ present in the undoped CeO₂ samples (which is ~17 vs. 25% La at the lowest La dopings, see Table 4), the La doping results in the formation of additional defects in the oxygen sublattice along with an increasing shift towards Ce⁴⁺ in the Ce content of the samples.

Based on these XPS observations, the TPR results can be understood based on two counter-acting trends with increasing La content: On one hand, the introduction of La increases the defect density in the oxygen sublattice, increasing oxygen mobility and hence the low-temperature reducibility of the mixed oxide. This is also in agreement with previous computational studies by Balducci et al., which show that ceria dopings can lower reduction energies and activation energies of oxygen migration [17, 23]. On the other hand, the increasing La content causes a decrease in the absolute number of reducible Ce⁴⁺ sites, which results in a decrease in hydrogen consumption in TPR. The interplay between these counter-acting phenomena results in a maximum in the H₂ consumption, reflecting an optimal composition for oxidation-reduction reactions, and hence indicates that a carefully controlled synthesis of mixed La/Ce oxides can result in promising materials for application in catalysis and related reactive applications.

Conclusions

Pure and mixed cerium and lanthanum oxides are the focus of much interest due to their increasingly wide application

in catalysis, absorption and related fields. Hence, there is a need to develop carefully controlled synthesis methods for such mixed oxides, and to establish clear correlations between structure, composition, and activity.

In the present study, we demonstrated the synthesis of mesoporous pure and mixed lanthanum and cerium oxides via a straightforward microemulsion-templated approach, resulting in materials with well-defined nanostructure and surface areas as high as ~110 m²/g at 450 °C. Most significantly, the carefully controlled microemulsion environment allowed the synthesis of highly homogeneous mixed La/Ce oxides across the entire composition range. Interestingly, all La_xCe_{1-x}O_{2-0.5x} crystallize in the fluorite structure of ceria, even for La contents as high as 90%. In addition to structural properties such as lattice parameter and particle size, varying the La content also allows fine tailoring of the reducibility of the samples due to the formation of oxygen vacancies upon incorporation of La in the ceria lattice.

The controllable pore size distribution along with tunable reducibility provides a promising avenue for tailored materials for catalysis and separation technology. We are currently extending the described approach beyond tailoring reducibility or oxygen storage capacity towards the introduction of carefully controlled multifunctionality, such as combination of catalytic and adsorptive properties.

Acknowledgements This work was supported by the National Energy Technology Laboratory's on-going research under the RDS contract DE-AC26-04NT41817; by the Department of Energy—Basic Energy Science through Grant DE-FG02-05ER46233; and by the National Science Foundation through Grant CTS-0553365. G.V. gratefully acknowledges a CNG faculty fellowship of the University of Pittsburgh's Swanson School of Engineering, and a faculty fellowship from DOE-NETL.

References

- Yan ZG, Yan CH (2008) J Mater Chem 18:5046
- Zhang D, Yoshioka F, Ikeue K, Machida M (2008) Chem Mater 20:6697
- Zou Z-Q, Meng M, Zha Y-Q, Liu Y (2008) J Mater Sci 43:1958. doi:[10.1007/s10853-008-2460-1](https://doi.org/10.1007/s10853-008-2460-1)
- Suda A, Yamamura K, Morikawa A, Nagai Y, Sobukawa H, Ukyo Y, Shinjo H (2008) J Mater Sci 43:2258. doi:[10.1007/s10853-007-2111-y](https://doi.org/10.1007/s10853-007-2111-y)
- Flytzani-Stephanopoulos M, Sakbodin M, Wang Z (2006) Science 312:1508
- Wang Z, Flytzani-Stephanopoulos M (2005) Energy Fuels 19:2089
- Chang JR, Chang SL, Lin TB (1997) J Catal 169:338
- Leckel D (2009) Energy Fuels 23:2370
- Nunan JG, Robota HJ, Cohn MJ, Bradley SA (1992) J Catal 133:309
- de Leitenburg C, Trovarelli A, Llorca J, Cavani F, Bini G (1996) Appl Catal A 139:161
- Kaspar J, Fornasiero P, Graziani M (1999) Catal Today 50:285

12. Fu Q, Weber A, Flytzani-Stephanopoulos M (2001) *Catal Lett* 77:87
13. Gennequin C, Lamallem M, Cousin R, Siffert S, Idakiev V, Tabakova T, Aboukaïs A, Su B (2009) *J Mater Sci* 44:6654. doi: [10.1007/s10853-009-3631-4](https://doi.org/10.1007/s10853-009-3631-4)
14. Park JB, Graciani J, Evans J, Stacchiola D, Ma S, Liu P, Nambu A, Sanz JF, Hrbek J, Rodriguez JA (2009) *Proc Natl Acad Sci USA* 106:4975
15. Bae JS, Choo WK, Lee CH (2004) *J Eur Ceram Soc* 24:1291
16. Balducci G, Islam MS, Kaspar J, Fornasiero P, Graziani M (2003) *Chem Mater* 15:3781
17. Balducci G, Kaspar J, Fornasiero P, Graziani M, Islam MS (1998) *J Phys Chem B* 102:557
18. Zhao X, Chen F, You J, Li X, Lu X, Chen Z (2010) *J Mater Sci* 45:3563. doi: [10.1007/s10853-010-4399-2](https://doi.org/10.1007/s10853-010-4399-2)
19. HartmanovÁ M, Lomonova E, Navrátil V, ŠUutta P, Kundracik F (2005) *J Mater Sci* 40:5679. doi: [10.1007/s10853-005-2795-9s](https://doi.org/10.1007/s10853-005-2795-9s)
20. Abanades S, Legal A, Cordier A, Peraudeau G, Flamant G, Julbe A (2010) *J Mater Sci* 45:4163. doi: [10.1007/s10853-010-4506-4](https://doi.org/10.1007/s10853-010-4506-4)
21. Qiao D, Lu G, Mao D, Guo Y, Guo Y (2010) *J Mater Sci*. doi: [10.1007/s10853-010-4786-8](https://doi.org/10.1007/s10853-010-4786-8)
22. Hosono E, Kujihara S (2004) *Chem Commun* 2062
23. Balducci G, Islam MS, Kaspar J, Fornasiero P, Graziani M (2000) *Chem Mater* 12:677
24. Wilkes MF, Hayden P, Bhattacharya AK (2003) *J Catal* 219:305
25. Ryan KM, McGrath JP, Farrell RA, Neill WMO, Barnes CJ, Morris MA (2003) *J Phys: Condens Matter* 15:L49
26. Dikmen S, Shuk P, Greenblatt M (1999) *Solid State Ionics* 126:89
27. Harrison PG, Kelsall A, Wood JV (1998) *J Sol-Gel Sci Technol* 13:1049
28. Morris BC, Flavell WR, Mackrodt WC, Morris MA (1993) *J Mater Chem* 3:1007
29. Belliere V, Joorst G, Stephan O, de Groot FMF, Weckhuysen BM (2006) *J Phys Chem B* 110:9984
30. Pileni MP (1997) *Langmuir* 13:3266
31. Fanun M (2009) *Microemulsions: properties and applications*. CRC Press, Boca Raton
32. Zarur AJ, Ying JY (2000) *Nature* 403:65
33. Schicks J, Neumann D, Specht U, Veser G (2003) *Catal Today* 81:287
34. Kirchhoff M, Specht U, Veser G (2005) *Nanotechnology* 16:S401
35. Sanders T, Papas P, Veser G (2008) *Chem Eng J* 142:122
36. Lyons DM, Harman LP, Morris MA (2004) *J Mater Chem* 14:1976
37. Sheng J, Zhang S, Lv S, Sun W (2007) *J Mater Sci* 42:9565. doi: [10.1007/s10853-007-2064-1](https://doi.org/10.1007/s10853-007-2064-1)
38. Lacombe S, Geantet C, Mirodatos C (1995) *J Catal* 151:439
39. Luo X, Wang R, Ni J, Lin J, Lin B, Xu X, Wei K (2009) *Catal Lett* 133:382
40. Bernal S, Botana FJ, García R, Rodríguez-Izquierdo JM (1987) *React Solid* 4:23
41. Mekheme GAH, Balboul BAA (2001) *Colloids Surf A* 181:19
42. Sing KSW, Everett DH, Haul RAW, Moscou L, Pierotti RA, Rouquerol J, Siemieniewska T (1985) *Pure Appl Chem* 57:603
43. Lowell S, Shields JE, Thomas MA, Thommes M (2004) *Characterization of porous solids and powders: surface area, pore size and density*. Kluwer Academic Publishers, Dordrecht
44. Thurber A, Reddy KM, Shutthanandan V, Engelhard MH, Wang C, Hays J, Punnoose A (2007) *Phys Rev B* 76:165206
45. Zhou XD, Huebner W (2001) *Appl Phys Lett* 79:3512
46. Patil S, Seal S, Guo Y, Schulte A, Norwood J (2006) *Appl Phys Lett* 88:243110
47. Dutta G, Waghmare UV, Baidya T, Hegde MS, Priolkar KR, Sarode PR (2006) *Chem Mater* 18:3249
48. Terribile D, Trovarelli A, de Leitenburg C, Dolcetti G, Llorca J (1997) *Chem Mater* 9:2676
49. Wang X, Lu G, Guo Y, Jiang L, Guo Y, Li C (2009) *J Mater Sci* 44:1294. doi: [10.1007/s10853-009-3275-4](https://doi.org/10.1007/s10853-009-3275-4)
50. Si R, Flytzani-Stephanopoulos M (2008) *Angew Chem Int Ed* 47:2884
51. Burroughs P, Hamnett A, Orchard AF, Thornton G (1976) *J Chem Soc, Dalton Trans* 1686
52. Trovarelli A (2002) *Catalysis by ceria and related materials*. Imperial College Press, London